Supplemental material of "Three-dimensional helical-rotating plasma structures in beam-generated partially magnetized *E*×*B* plasmas"

Jian Chen[1, *], Andrew T. Powis[2], Igor D. Kaganovich[2], Zhibin Wang[1, *], Yi Yu[1, *]

[1]*Sino-French Institute of Nuclear Engineering and Technology, Sun Yat-sen University, Zhuhai 519082, P. R. China*

[2]*Princeton Plasma Physics Laboratory, Princeton NJ 08540, USA*

*Emails: chenjian5@mail.sysu.edu.cn, wangzhb8@mail.sysu.edu.cn and yuyi56@mail.sysu.edu.cn

Contents

I. Fourier spectrum of the helical plasma structure

Figs. S1(a)~(c) depict the "camera" view of the helical-rotating plasma structure at different times, showing the projected electron density. The dynamics resemble an m=1 azimuthal spoke, which could potentially lead to a misinterpretation of this

structure in some experiments. Fig. S1(d) displays the Fourier spectrum of the electron density fluctuations caused by the rotation of the helical plasma structure, exhibiting a pronounced frequency around $\omega \approx 5.6$ MHz.

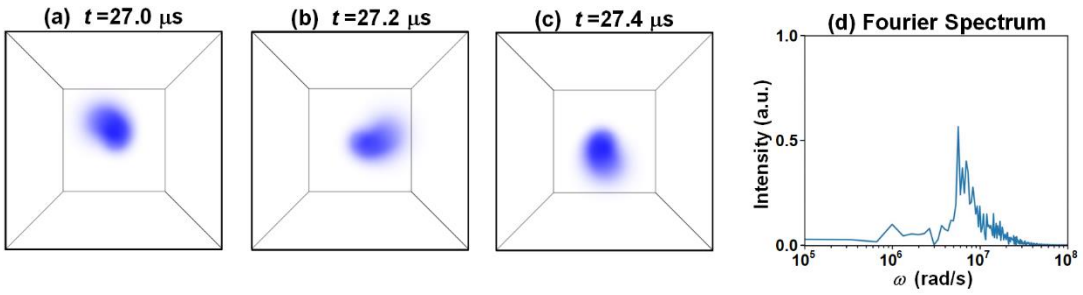

Fig. S1 Subfigures (a), (b) and (c) depict the end views of the helical-rotating plasma structure at t=27.0 μs, t=27.2 μs and t=27.4 μs, respectively. The end views are captured by a synthetic diagnostic "camera" located near the end of the domain with a 30° view angle. Black lines mark the boundaries (gray lines mark the 30° view angle boundaries). Subfigure (d) presents the Fourier spectrum of electron density fluctuation caused by the rotation of the helical plasma structure. The electron density data used in the Fourier transformation were recorded by a probe at the point (0.4 cm, 2.0 cm, 0 cm). All the data were recorded from the case with p=1 mTorr.

II. Transverse ion loss due to centrifugal forces in the non-neutral regime

In an electron beam-plasma discharge, the negative charge of the electron beam creates a potential well which confines ions produced by ionization. This leads to an increasing ion density over time and ultimately the formation of a quasi-neutral plasma. However, we observed that at lower pressure, an ambipolar quasi-neutral plasma does not form, and offer an explanation for this observation here. Figs. S2(a)~S2(c) show that not only electrons but also ions collectively rotate off the beam axis. This rotation is induced as ions experience kicks caused by the rotating potential well generated by the net negative charge of the electron beam. Therefore, the ion flux is driven by two competing effects: the action of the inward electric field produced by the negative space charge of the electron beam and by an outward directed centrifugal force.

As the helical plasma rotates off-axis azimuthally, newly-produced ions experience an outward centrifugal force that ejects them from the potential well. The

effective potential including the centrifugal potential reads

$$\phi^* = \phi + \phi_{centrifugal} = \phi - \frac{m_i \omega^2 r^2}{2e}, \tag{S1}$$

where $\omega \approx 5.6$ MHz denotes the angular frequency of the helical plasma structure. The effective potential profile is shown in Figs. S2(d)~S2(f), where the solid circles indicate the high ion density regions, corresponding to the density profiles in Figs. S2(a)~S2(c). The effective potential, ϕ^*, decreases outwards - as indicated by the arrow - confirming that ions can escape toward the walls. Note that the gradient of ϕ^* also has an azimuthal component, providing evidence that the kick of ions by the rotating potential well contributes to ion rotation.

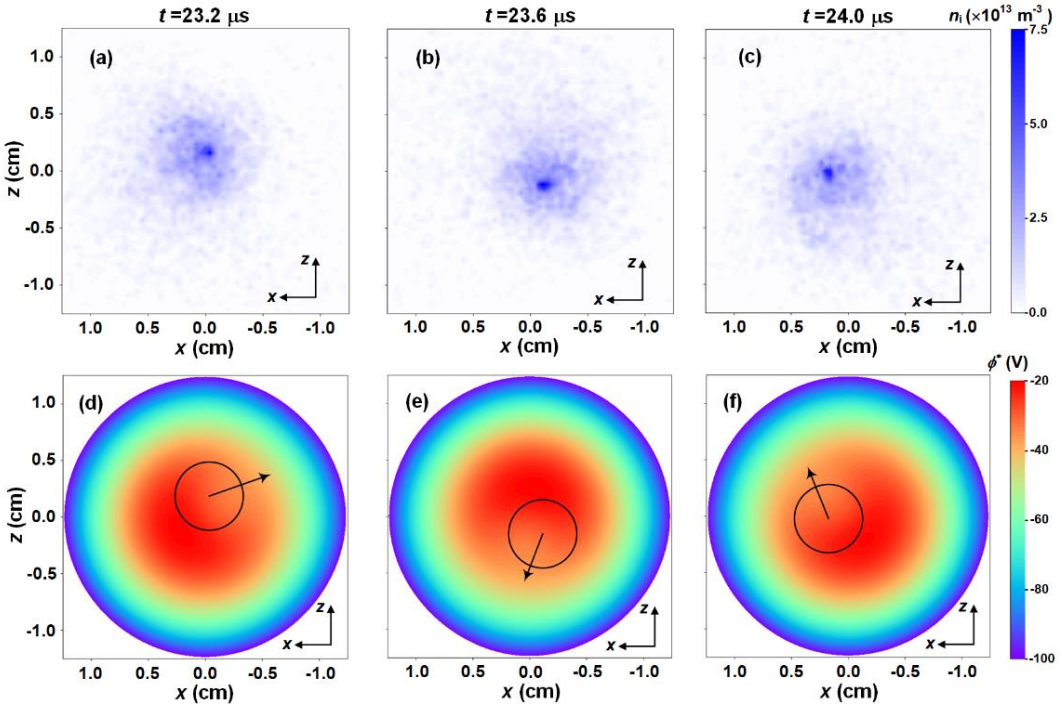

Fig. S2 Profiles of ion number density and effective potential profile $\phi^*=\phi - m_i\omega^2 r^2/2e$ at y=10 cm at different snapshots for the case with p=1 mTorr (non-neutral regime). The solid circles, delineate the high ion density regions shown in (a)-(c), and arrows indicates the direction of decreasing ϕ^*.

III. Parameters used for calculating the dispersion relation

The local simulation parameters used in calculating the dispersion relation of the lower-hybrid instability (see Fig. 2(b) in the main text) are summarized in Table S1.

Table S1. Local parameters used in the calculation of dispersion relation of low-hybrid instability

Parameters	n_0 (m^{-3})	T_e (eV)	B_0 (Gauss)	L_n (cm)	E_r (V/m)	ν_{en} (s^{-1})
Values	1.5×10^{15}	10	100	-0.25	-1000	1.2×10^{7}

IV. Profile of Λ triggering the diocotron instability

Fig. S3 shows the radial profile of Λ (see Eq. (5) in the main text) at y=0.02 cm for the case with p=1 mTorr. The profile of Λ was calculated using the averaged electron and ion density profiles over the first 200 nanoseconds of the simulation. The transverse plane y=0.02 cm was selected because it marks the location where the diocotron instability initiates and begins to split the beam. As one can see, Λ crosses zero at approximately r≈0.32 cm, indicating that the diocotron instability can be triggered at this radius due to resonance (as confirmed by Fig. 3(b) in the main text).

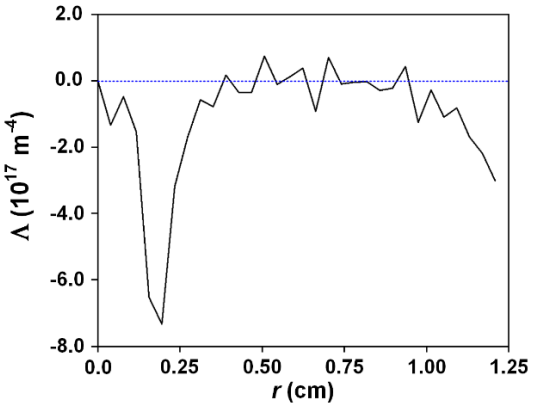

Fig. S3 Radial profile of Λ at y=0.02 cm for the case with p=1 mTorr. The profile of Λ was calculated using the time averaged electron and ion density profiles over the first 200 nanoseconds.

V. Instability-enhanced diffusion in the quasi-neutral regime

As explained in the main text, the quasi-neutral and non-neutral regimes are primarily distinguished by the quasi-neutrality condition (whether it is attained or not). Therefore, the value of the threshold pressure delineating the two regimes can be regarded as the minimum pressure at which quasi-neutrality is maintained, and can be analyzed via transport calculations in the quasi-neutral regime.

Fig. S4 shows the electron and ion number density profiles, as well as the

electrostatic potential at quasi-steady state for the case with p=10 mTorr, corresponding to the quasi-neutral regime. In this regime, the density exhibits an exponentially decreasing profile. Within the central region (r<0.75 cm), the mean electric field remains relatively weak, whereas a strong fluctuating electric field is observed, resulting in instability-enhanced radial diffusion of particles. While at the periphery (r>0.75 cm), a mean electric field emerges, accelerating ions.

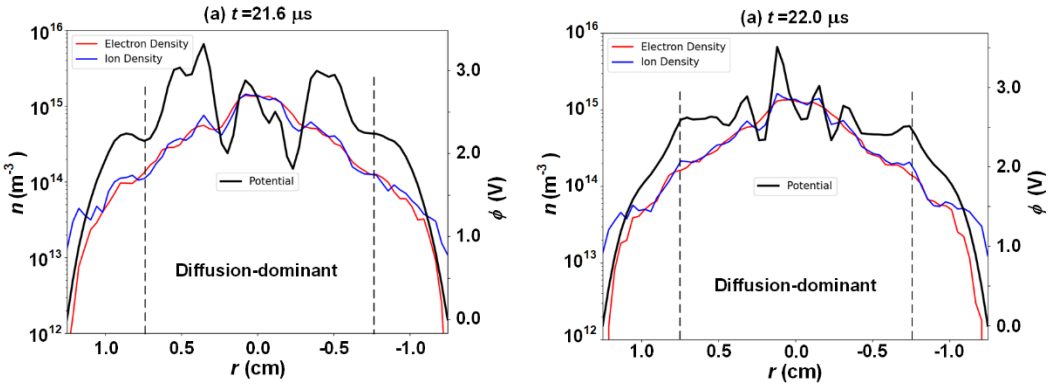

Fig. S4 Profiles of electron and ion number densities and electrostatic potential for the quasi-steady state case with p=10 mTorr. In the central region (r<0.75 cm, approximately 3|L_n|), a strong fluctuating electric field is observed and the radial ion transport is dominated by the instability-enhanced diffusion. At the periphery, a mean electric field emerges, accelerating ions and leading to mobility-dominated transport.

At quasi-steady state, the ion balance gives

$$n_b \nu_{iz} S_{beam} = \Gamma_{ir} \cdot S, \tag{S2}$$

where ν_{iz} represents the electron-impact ionization coefficient, S_{beam} is the area of the beam cross section, Γ_{ir} is the outward radial ion flux and S=2πr is the enclosed surface area. Here, it is assumed that ions are predominantly generated via beam electron-impact ionization and lost through radial transport. Such assumptions neglect the ionization caused by the beam-produced plasma electrons and ion loss through the front and end walls, which is acceptable for the large aspect ratio of our system.

Considering the radial transport shown in Fig. S4, the ion balance equation can be simplified by focusing on the enclosed surface within the diffusion-dominated region and assuming an exponentially decreasing density profile. This yields Eq. (6) in the

main text

$$n_b \nu_{iz} S_{beam} = D_\perp n_{i0} \exp\left(-\frac{r}{|L_n|}\right) \cdot \frac{2\pi r}{|L_n|}, \tag{S3}$$

where $L_n = n_0 / n_0'$ is the gradient length and $D_\perp$ is the perpendicular diffusion coefficient. It should be noted that $D_\perp$ varies with radius to ensure continuity, which has been confirmed in recent experiments [2].

VI. Estimating the rotation frequency of the helical structure using the image method

The first step in estimating the rotation frequency of the helical structure is to determine the effective electric field $\boldsymbol{E}_{eff}$ acting on the plasma. This effective electric field arises primarily from the asymmetric charge distribution caused by the off-axis rotation of the plasma, which can be estimated using the image method.

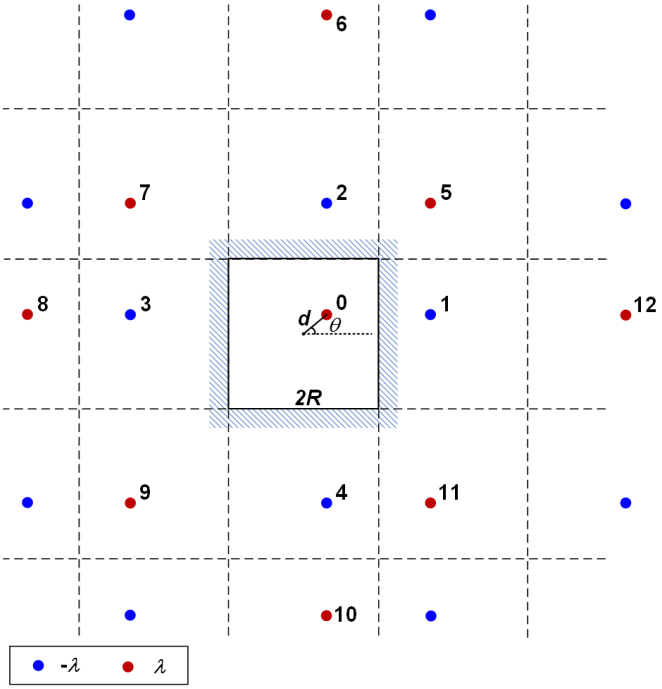

Fig. S5 Charge images for a real line charge in a square box. The red and blue dots denote the line charges with λ and -λ, respectively.

For the cases considered in this study, where the pitch of the helical plasma is much larger than the eccentricity d, the system can be modeled as a long line charge

(Charge 0) with linear charge density $\lambda \approx -\int e\left(n_e - n_i\right)\mathrm{d}S$ confined within a square box, as shown in Fig. S5. This configuration leads to an infinite number of image charges, created by reflecting both the real and image charges and flipping their signs with each reflection. The red and blue dots denote the line charges with λ and -λ, respectively.

Let the real charge (Charge 0) have the coordinate $\boldsymbol{r}_0 = d\cos\theta\boldsymbol{e}_x + d\sin\theta\boldsymbol{e}_y$. Then, the coordinates of the images with λ and -λ are given by

$$\begin{cases} \boldsymbol{r}_{-\lambda} = \begin{cases} \left(4mR + 2R - d\cos\theta\right)\boldsymbol{e}_x + \left(4nR + d\sin\theta\right)\boldsymbol{e}_y \\ \left(4mR + d\cos\theta\right)\boldsymbol{e}_x + \left(4nR + 2R - d\sin\theta\right)\boldsymbol{e}_y \end{cases} \\ \boldsymbol{r}_{\lambda} = \begin{cases} \left(4mR + d\cos\theta\right)\boldsymbol{e}_x + \left(4nR + d\sin\theta\right)\boldsymbol{e}_y \\ \left(4mR + 2R - d\cos\theta\right)\boldsymbol{e}_x + \left(4nR + 2R - d\sin\theta\right)\boldsymbol{e}_y \end{cases} \end{cases}, \; m, n \in \mathbb{Z} \text{ and } (m,n) \neq (0,0), \tag{S4}$$

where R is half of the side length of the square box, m and n are arbitrary integers. m and n cannot both be zero, as this would correspond to the position of the real charge itself. The effective electric field $\boldsymbol{E}_{eff}$ is then the superposition of the fields generated by all the image charges on the real charge (Charge 0)

$$\boldsymbol{E}_{eff} = \sum_{m,n\in\mathbb{Z},(m,n)\neq(0,0)}^{\infty} \left(\frac{\lambda\left(\boldsymbol{r}_{\lambda} - \boldsymbol{r}_0\right)}{2\pi\varepsilon_0\left|\boldsymbol{r}_{\lambda} - \boldsymbol{r}_0\right|^2} - \frac{\lambda\left(\boldsymbol{r}_{-\lambda} - \boldsymbol{r}_0\right)}{2\pi\varepsilon_0\left|\boldsymbol{r}_{-\lambda} - \boldsymbol{r}_0\right|^2} \right). \tag{S5}$$

The calculation can be simplified by considering only the contributions from the nearest images, specifically those formed by one- and two-time reflections (i.e., Charges 1~12 in Fig. S5). These nearest images are the most significant because the electric field decays with distance.

It is readily proved that the electric field generated by the four one-time-reflection images (Charges 1~4) is

$$\boldsymbol{E}_{1\sim4} = -\frac{\lambda}{2\pi\varepsilon_0}\frac{d\cos\theta}{\left(R^2 - d^2\cos^2\theta\right)}\boldsymbol{e}_x - \frac{\lambda}{2\pi\varepsilon_0}\frac{d\sin\theta}{\left(R^2 - d^2\sin^2\theta\right)}\boldsymbol{e}_y. \tag{S6}$$

The electric field due to the eight two-time-reflection images (Charges 5–12) is

$$\boldsymbol{E}_{5\sim12} = \frac{\lambda}{2\pi\varepsilon_0}\frac{d^3\sin\theta\sin 2\theta}{\left(R^4 - d^4\sin^2 2\theta\right)}\boldsymbol{e}_x + \frac{\lambda}{2\pi\varepsilon_0}\frac{d\cos\theta\sin 2\theta}{\left(R^4 - d^4\sin^2 2\theta\right)}\boldsymbol{e}_y. \tag{S7}$$

For the cases investigated in this work, R is typically several times larger than d.

Therefore, the contribution from the images in the second reflection group (Charges 5–12) is negligible (on the order of d^2/R^2 relative to $\boldsymbol{E}_{1\sim4}$), allowing us to approximate the effective electric field as:

$$\boldsymbol{E}_{eff} \approx -\frac{\lambda}{2\pi\varepsilon_0}\frac{d\cos\theta}{R^2}\boldsymbol{e}_x - \frac{\lambda}{2\pi\varepsilon_0}\frac{d\sin\theta}{R^2}\boldsymbol{e}_y, \tag{S8}$$

where the d^2 term in the denominator has been omitted. Eq. (S8) shows that $\boldsymbol{E}_{eff}$ points in the radial direction and generates the $\boldsymbol{E}_{eff}\times\boldsymbol{B}$ drift, which supports azimuthal rotation of the plasma. Consequently, the angular frequency of the helical plasma can be estimated as

$$\omega \approx \frac{|\lambda|}{2\pi\varepsilon_0 BR^2}. \tag{S9}$$

Note that Eq. (S9) gives the same estimate as that derived for a cylindrical chamber [3].

VII. Description of Supplemental videos

Supplemental videos I and II titled "10mTorr_3D" and "1mTorr_3D" show the 3D views of electron number density for the cases with p=10 mTorr and p=1 mTorr.

Supplemental videos III and IV titled "10mTorr_end" and "1mTorr_end" show the end views of electron number density for the cases with p=10 mTorr and p=1 mTorr.

Reference

[1] Y. Yu, C. Y. Xiao, H. Liu, Z. H. Wang, Y. X. Zhou, G. Y. Zhao, M. Xu, L. Nie, Z. H. Yuan, and P. F. Zheng, JINST **19**, P02020 (2024).

[2] N. S. Chopra, Boundary-induced kinetic effects in low temperature E×B plasmas, Ph.D. thesis, Princeton Univerisity, 2024.

[3] K. S. Fine, Phys. Fluids B **4**, 3981 (1992).